PNAS RESEARCH ARTICLE | NEUROSCIENCE OPEN ACCESS

# ECgo: All-optical induction of single endothelial cell injury and capillary occlusion in the brain

Jacqueline Condrau[a,b,1], Srinivasa R. Allu[c,d,1], Tatiana V. Esipova[c,d,2], Eva Erlebach[a,b], Matthias T. Wyss[a,b], Chaim Glück[a,b], Luca Ravotto[a,b], Thomas Troxler[c,d], Mikhail Drobizhev[e], Marco Villa[f], Paola Ceroni[f], Mohamad El Amki[b,g], Sergei A. Vinogradov[c,d,3], and Bruno Weber[a,b,3]

Affiliations are included on p. 9.

Edited by Patrick J. Drew, The Pennsylvania State University, University Park, PA; received May 27, 2025; accepted April 6, 2026 by Editorial Board Member Mark T. Nelson

**The ability to induce endothelial cell (EC) damage in the mouse brain with high spatial precision is invaluable for mechanistic studies of brain capillary injury and repair. Here, we introduce an optical method, termed Endothelial Cell guided obliteration (ECgo), that utilizes a two-photon-excitable porphyrin-based photosensitizer (*Ps2P*) to selectively obliterate single ECs within the brain microvascular network. Using the developed approach, we were able to induce occlusions of single capillaries with high spatiotemporal control, while preserving the surrounding tissue. Combined with longitudinal two-photon imaging, ECgo enables studies of morphological and functional consequences of targeted single capillary EC injury in vivo under healthy and diseased conditions.**

cerebral blood flow | brain capillaries | microstroke | porphyrins | photodynamic therapy

Brain capillaries constitute over 80% of the cerebral vasculature and are essential for maintaining proper brain function. While occlusions of penetrating arteries and ascending veins can disrupt blood supply and homeostasis in large brain tissue regions (1–5), the impact of single capillary injury and subsequent occlusion remains understudied. Notably, capillary occlusions have been observed in patients with cerebrovascular and neurological conditions, including stroke (6, 7), cerebral microinfarcts (8, 9), Type 1 diabetes (10, 11), vascular dementia (12), and Alzheimer's disease (13, 14), underscoring the need for a better understanding of their pathophysiology. Furthermore, microvascular pathology is hypothesized to both precede and contribute to age-related cognitive decline and neurodegenerative conditions (15, 16).

Multiple experimental approaches have been used to induce capillary occlusions, including vascular injection of small occlusive microspheres (17–19) as well as optical methods, such as laser-induced injury (11, 20, 21) and photothrombosis using Rose Bengal (22–24). However, these approaches lack the ability to create microvascular lesions with sufficient spatiotemporal accuracy, frequently leading to extensive nonlocal vascular injuries. Achieving precise, single-capillary occlusion in the living mouse brain remains technically challenging, hindering efforts to explore the molecular and cellular dynamics of capillary injury and repair across the interconnected neuron–glia–vasculature network.

Here, we report the development of a technique termed Endothelial Cell guided obliteration (ECgo) that allows targeting of single capillaries by inducing endothelial cell (EC) damage with high spatiotemporal control. ECgo makes use of a two-photon-excitable photosensitizer (termed *Ps2P*), based on the Zn complex of tetraarylphthalimidoporphyrin (TAPIP), which is closely related, both structurally and spectroscopically, to the two-photon (2P) oxygen probe Oxyphor 2P developed by us previously (25). Unlike in disease-progressed states, where multiple capillaries are already damaged, ECgo makes it possible to create a single brain capillary occlusion to investigate its early impact, while avoiding the complexity of widespread vascular injury.

## Results

**Development of the Two-Photon Photosensitizer *Ps2P*.** Photosensitization processes and associated cell damage underpin photodynamic therapy (PDT), an established clinical modality (26, 27). The photodynamic effect (Fig. 1*A*) entails photoexcitation of a photosensitizer compound (Ps), usually to its lowest singlet excited state ($S_1$), followed by a fast (pico- to nanosecond) intersystem crossing (*isc*) with the formation of the Ps triplet state ($T_1$). The $T_1$ state is usually long-lived (μs), and, therefore, prior to its spontaneous deactivation (associated with rate constant *k* in Fig. 1*A*), it can undergo diffusional encounters and subsequent reactions

## Significance

Brain capillary injury is a common feature of aging and many neurological disorders. While a single capillary lesion may appear inconsequential, the cumulative effect of repeated and spatially dispersed capillary insults can lead to substantial brain dysfunction. Understanding how single capillary injuries contribute cumulatively to long-term brain damage requires tools that can precisely target individual capillaries in the living brain. Here, we introduce an optical method based on a light-activatable compound to selectively injure single brain capillaries with high spatial accuracy. Our method enables detailed, longitudinal studies of capillary repair, blood flow recovery, local oxygen dynamics, and glial responses following microvascular injury.

Author contributions: J.C., E.E., M.T.W., C.G., M.E.A., S.A.V., and B.W. designed research; J.C., S.R.A., T.V.E., E.E., C.G., T.T., M.D., and S.A.V. performed research; S.R.A., T.V.E., T.T., M.V., P.C., and S.A.V. contributed new reagents/analytic tools; J.C., S.R.A., T.V.E., E.E., C.G., L.R., T.T., M.D., and S.A.V. analyzed data; and J.C., M.T.W., M.E.A., S.A.V., and B.W. wrote the paper.

The authors declare no competing interest.

This article is a PNAS Direct Submission. P.J.D. is a guest editor invited by the Editorial Board.



[1]J.C. and S.R.A. contributed equally to this work.

[2]Present address: Department of Chemistry, Loyola University Chicago, Chicago, IL 60660.

[3]To whom correspondence may be addressed. Email: vinograd.upenn@gmail.com or bweber@pharma.uzh.ch.

This article contains supporting information online at https://www.pnas.org/lookup/suppl/doi:10.1073/pnas.2513515123/-/DCSupplemental.

Published May 18, 2026.

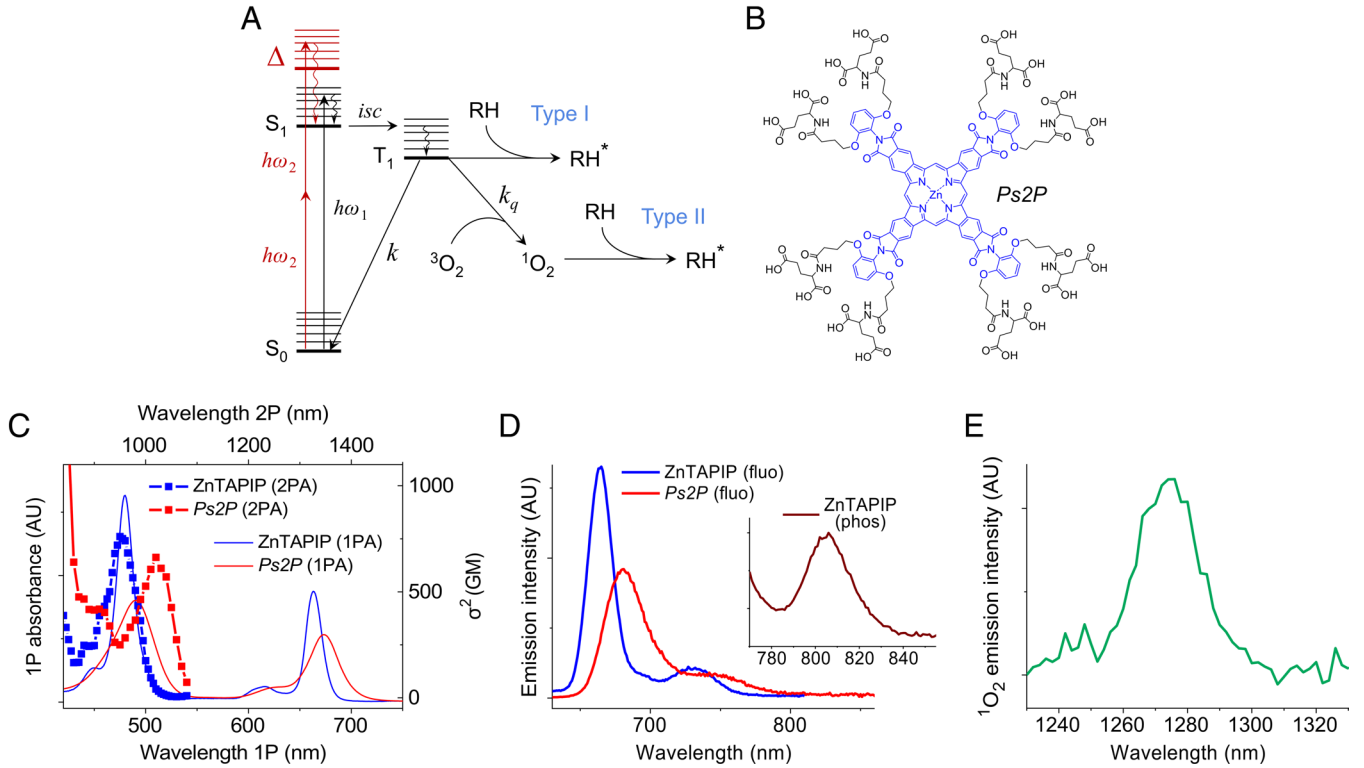


**Fig. 1.** (*A*) Energy diagram showing one-photon (1P) ($h\omega_1$) excitation of a photosensitizer to its lowest excited singlet state ($S_1$), followed by the *isc* to the triplet state ($T_1$), which reacts with biomolecules (RH) directly (Type I PDT), or sensitizes molecular oxygen, which subsequently reacts with biomolecules (Type II PDT), causing their damage. The 2P excitation pathway as shown ($2 \times h\omega_2$; marked in red) is characteristic of porphyrins structurally similar to ZnTAPIP, in which the lowest 2P active state Δ is located energetically above the Q state ($S_1$), but below the *B* state. (*B*) Structure of the photosensitizer *Ps2P*. The parent Zn tetraarylphthalimidoporphyrin (ZnTAPIP) is shown in blue. (*C*) 1PA and 2PA spectra of ZnTAPIP in N-methylpyrrolidone (NMP) (blue) and *Ps2P* (red). 1PA spectrum of *Ps2P* was recorded in aq. buffer (pH 7.3), while its 2PA spectrum was measured in $D_2O$. (*D*) Fluorescence spectra of ZnTAPIP in aerated NMP (blue) and *Ps2P* in aerated aq. buffer, pH 7.3 (red) ($\lambda_{ex}$ = 620 nm). The integrated emission intensities are normalized to unity. *Inset*: phosphorescence of ZnTAPIP in deoxygenated NMP. (*E*) Singlet oxygen emission sensitized upon irradiation of *Ps2P* in $D_2O$ at 475 nm.



with molecules in the environment. Direct interactions of the triplet with biological molecules (shown as RH in Fig. 1*A*; where RH represents a generic organic substrate, and RH* refers to damaged, usually oxidized, species) fall under the umbrella of reactions classified as PDT Type I [electron transfer processes (28)]. Since both the biomolecule and the sensitizer are typically large, slowly diffusing species, this mechanism usually requires close proximity of the Ps molecule to a biological target prior to photoexcitation.

Another more common mechanism, known as PDT Type II, involves energy transfer from the Ps triplet to the ground state molecular oxygen ($^3O_2$), resulting in the conversion of the latter to its singlet state. Singlet oxygen ($^1O_2$) is a rapidly diffusing, highly reactive species [lifetime ~3.5 μs in $H_2O$ at ambient temperatures (29)] that can readily oxidize almost any molecule in the biological milieu. Thus, contributions of Type I via direct oxidation of organic targets and Type II pathways to the overall photodamage depend on the availability of $O_2$, with Type II being the dominant pathway under normoxic conditions.

The combination of photosensitization with 2P excitation gives rise to a 2P photodynamic effect (30, 31), whereby 2P excitation makes it possible to confine photodamage to the immediate vicinity of the laser focus, permitting targeting of microscopic regions many microns deep in the tissue. For example, 2P excitation of a popular sensitizer Rose Bengal has been used to create targeted damage in the brain (3, 4, 32).

Porphyrins and phthalocyanines form a prominent group of photosensitizers due to their well-documented ability to generate triplet states (33). However, thanks to their centrosymmetric structures, regular cyclic tetrapyrroles typically possess extremely low two-photon absorption (2PA) cross-sections in the spectral region suitable for in vivo optical excitation. Much effort has been devoted over the years to the enhancement of 2PA in porphyrins and related compounds. A number of molecular systems have been developed that are able to act as efficient 2P absorbers and simultaneously singlet oxygen sensitizers. One relevant example is a porphyrin dyad with the peak 2PA cross-section ($\sigma^{(2)}$) of ~17,000 GM at 920 nm (Göppert-Mayer units: 1GM = $10^{-50}$ $cm^4$ s), which has been successfully used to occlude a single pial artery in the brain (34).

In our previous work, we used aromatic π-extension combined with substitution by electron-withdrawing groups as a means to stabilize 2P-active *gerade* symmetry states (*g*-states) in porphyrins, creating compact, highly 2P-active porphyrinoids (35, 36). The Pt(II) complex of one such porphyrin, Pt tetraarylphthalimidoporphyrin (PtTAPIP), was used to construct a high-performance 2P oxygen probe Oxyphor 2P (25). Due to the strong heavy metal-induced spin–orbit coupling, $S_1 \rightarrow T_1$ *isc* (Fig. 1*A*) in Pt and Pd porphyrins is extremely fast (picoseconds), and the triplet states are formed with nearly unity efficiency. However, the same spin–orbit coupling accelerates both radiative and nonradiative decays (rate constant *k* in Fig. 1*A*) of the triplet ($T_1 \rightarrow S_0$), effectively shortening its lifetime, which varies from tens to hundreds of microseconds (μs) for e.g., Pt and Pd TAPIPs, respectively (36). We reasoned that using a lighter metal, such as Zn, could be beneficial for photochemical reactions involving the triplet state (both Type I and II pathways; Fig. 1*A*) since weaker spin–orbit coupling should elongate the $T_1$ lifetime and thus increase the probability of diffusional encounters and subsequent photochemical transformations. Importantly, Zn is still able to promote efficient $S_1 \rightarrow T_1$ *isc* in

porphyrins (albeit not as efficient as heavier metals) while not fully eliminating fluorescence, which is instrumental for imaging photosensitizer distributions in biological tissue.

The structure of the 2P photosensitizer developed in this work, termed *Ps2P*, is shown in Fig. 1*B*. *Ps2P* is ZnTAPIP modified at the periphery with eight glutamic acid residues. The electronic absorption spectrum of the parent porphyrin, recorded in NMP, shows a familiar pattern consisting of two narrow transitions, Q (662 nm) and B or Soret (475 nm) bands, which are bathochromically shifted compared to the respective transitions of Pt and Pd TAPIPs (36). The 16 carboxylate groups are able to solubilize *Ps2P* in aqueous media, although the corresponding absorption spectrum (Fig. 1*C*) clearly shows signs of aggregation, manifested by broadening and bathochromic shifts of the absorption bands (490 and 673 nm for B and Q bands, respectively) relative to the spectrum of the parent porphyrin (Fig. 1*C*).

The 2PA spectrum of *Ps2P* was measured in $D_2O$, which has significantly weaker absorption near 900 to 1000 nm. The key spectral feature is the transition to a strongly 2P-allowed state ($\lambda_{max}$ ~ 1020 nm), which is reminiscent of the bands seen in the 2PA spectra of Oxyphor 2P (25) as well as of parent Pt and Pd TAPIPs (36). This *g*-symmetry state, termed Δ-state (37), is forbidden for 1P excitation, since the ground state in ZnTAPIP is also a *g*-state. Hence, the Δ-state is not seen in the 1PA spectra. The energy of the Δ-state is below that of the 1P-allowed B (Soret) state. The strong 2PA to the blue of the Δ-peak allowed us to carry out efficient off-peak 2P photosensitization and oxygen measurements using Oxyphor 2P without changing the laser wavelength. The 2PA maximum of Oxyphor 2P is near 960 nm, while at 1020 nm, its absorption is very low (25).

Both *Ps2P* and its parent ZnTAPIP exhibit prompt and thermally activated (E-type) delayed fluorescence (TADF). In aerated NMP, ZnTAPIP fluoresces ($\lambda_{max}$ = 665 nm) with a quantum yield ($\phi_{fl}$) of 0.14, showing a clear single-exponential fluorescence decay ($\tau_{fl}$ = 1.81 ns). Upon deoxygenation, the fluorescence quantum yield rises up to 0.46, and an additional band emerges ($\lambda_{max}$ = 806 nm; Fig. 1*D*, *Inset*), which corresponds to $T_1 \rightarrow S_0$ phosphorescence ($\phi_{phos}$ ~ 0.015). The triplet lifetime obtained from either TADF (665 nm, $S_1 \rightarrow S_0$) or phosphorescence (806 nm, $T_1 \rightarrow S_0$) decays was found to be ~9.4 ms, suggesting that the triplet of ZnTAPIP is efficiently quenched by $O_2$. Indeed, no traces of emission could be detected in air-saturated solutions.

The fluorescence quantum yield of *Ps2P* in aerated PBS (phosphate buffer saline) was found to be reduced to 0.02, and the emission decay, which became profoundly nonsingle exponential, was considerably shortened ($\tau_{av}$ = 0.66 ns, $\lambda_{max}$ = 695 nm). The reduction in fluorescence is likely caused in part by aggregation. Indeed, upon dissolving *Ps2P* in PBS containing bovine serum albumin (BSA; 4% by weight), the spectral bands sharpened over time, and the fluorescence quantum yield increases by more than threefold, reaching ~0.07, showing that BSA helps to prevent the aggregation of *Ps2P* and suggesting that in the blood *Ps2P* is predominantly bound to albumin and/or other hydrophobic/amphiphilic components. From a practical point of view, the fluorescence of *Ps2P* is highly instrumental for visualizing its distribution in the vasculature.

Upon deoxygenation, the fluorescence quantum yield of *Ps2P* (in PBS) increases by ~10% (to ~0.022), and a long-lived emission (detected near 700 nm) appears with a lifetime of ~1.2 ms. While the phosphorescence of the *Ps2P* band could not be detected explicitly, the long-lived decay is most certainly a signature of its triplet state, which gives rise to the delayed fluorescence via reverse *isc* ($T_1 \rightarrow S_1$).

To verify that *Ps2P* is capable of a Type II photodynamic action, $^1O_2$ emission was recorded upon irradiation of a *Ps2P* solution at 475 nm (Fig. 1*C*). The quantum yield of $^1O_2$ was found to be ~0.2 {measured against standard sensitizer Eosin [$\phi(^1O_2)$ = 0.58]} (38). Given its relatively hydrophobic nature, *Ps2P* is likely to be bound to albumin and other proteins in the blood, but it could also be partially partitioned into the membranes of the ECs lining the capillaries. As such, upon photoexcitation, *Ps2P* could directly engage in photochemical processes with lipids and proteins in its vicinity according to the Type I mechanism. Importantly, the differences between the photophysical pathways leading to the triplet state upon 2P vs. 1P excitation have no effect on photodynamic efficiency, which usually simply scales with the number of photons absorbed, and hence it is proportional to the excitation rate at a selected wavelength.

***Ps2P* Enables Targeted Capillary Occlusion in the Brain.** Having characterized the chemical and photophysical properties of *Ps2P*, we next sought to evaluate its potential as a 2P excitable photosensitizer for inducing single capillary occlusions in the mouse brain. To visualize the vascular network, we first intravenously injected the dye Texas Red-dextran (70 kDa, 2.5% in aq. NaCl). Blood vessels were mapped through the cranial window at successive depths in the cortex, and the resulting images were used to construct a maximum intensity projection (MIP) image. Using the MIP image, several capillaries were selected for targeted occlusion based on their diameter (3 to 6 μm) and the depth from the surface (50 to 200 μm). In order to induce localized injury, *Ps2P* was injected intravenously (Fig. 2*A*) through a tail vein catheter (3 mg/mL in PBS; estimated blood concentration 30 μM; assumed blood amount 0.078 mL/g body weight) and 2P-excited by scanning the laser focus along the vessel midline of a selected capillary (2 to 3 μm-long line, average power 30 mW under the objective, 960 nm), until blood flow ceased. Red blood cell (RBC) velocity ($V_{RBC}$) in the capillary was measured before and after the irradiation scan (Fig. 2 *A*–*C*). The first indication of the injury was detected as a slow-down and subsequent cessation of RBC passage through the capillary, occurring on average ~60 s after the start of irradiation (Fig. 2 *A*–*C*). Note that in our experiments, irradiation was carried out at 960 nm, which is off-peak in the 2PA spectrum of *Ps2P* ($\lambda_{max}$ = 1,020 nm), because of potential concurrent or multiplexed 2P phosphorescence lifetime imaging of oxygen using Oxyphor 2P (25), whose 2PA maximum is at 960 nm.

In the absence of *Ps2P* or other dyes, even prolonged irradiation (300 s; other irradiation parameters unchanged) did not lead to capillary occlusion and/or injury, as verified by label-free THG imaging (Fig. 2*E*) (39, 40). Similarly, irradiation in the presence of conventional intravascular dyes, e.g., Texas Red-dextran (2.5% in aq. NaCl; 70 kDa), FITC dextran (2.5% in aq. NaCl; 70 kDa), or quantum dot-based vascular marker (Qtracker655™; 2 μM), under identical conditions (300 s, 30 mW under the objective, 960 nm), resulted neither in a reduction in $V_{RBC}$ nor in capillary stalling (25 capillaries tested; Fig. 2 *F* and *G*).

The key practical advantages of *Ps2P* were revealed in comparative tests against a commonly used photosensitizer Rose Bengal, whose 2PA spectrum was measured in independent experiments. To facilitate the comparison, irradiation was carried out using the same wavelength and laser power (1040 nm, 30 mW under the objective), while the concentrations of the sensitizers were adjusted, so that their 2P-absorbances matched at 1040 nm, where the 2PA cross-section of *Ps2P* is ~20 times larger than that of Rose Bengal. A much higher 2PA cross-section throughout the entire near-infrared region is the first marked advantage of *Ps2P* over Rose Bengal (*SI Appendix,* Fig. S2*C*), allowing for lower concentrations of the dye to be used in photosensitization experiments.

Under matched excitation conditions ($\lambda_{ex}$ = 1040 nm, concentrations adjusted according to the 2PA cross-sections, equal laser power), irradiation using either Ps2P or Rose Bengal led to capillary occlusions without rupture or any other detectable collateral damage

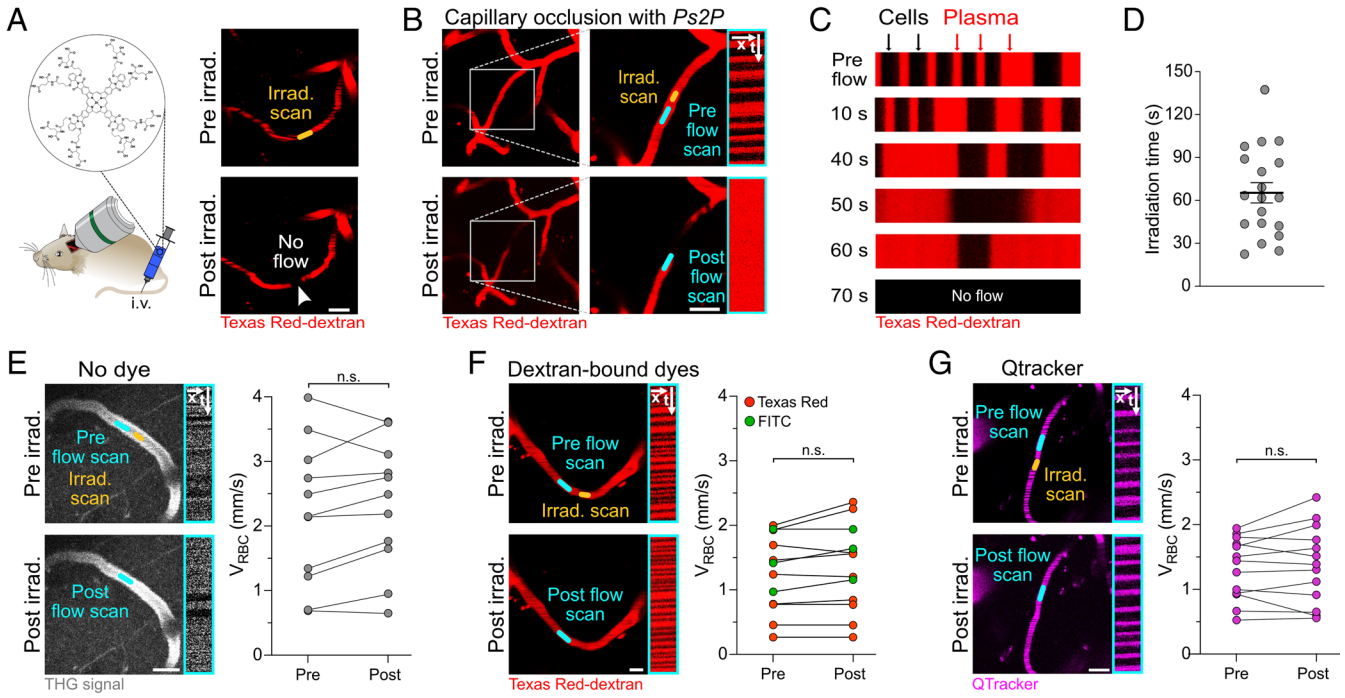


**Fig. 2.** (*A*) Cartoon illustrating injection of *Ps2P* and representative 2P fluorescence images of a capillary pre- and post irradiation. The white arrowhead points at the occluded capillary segment. (Scale bar, 10 μm.) (*B*) Representative maximum intensity 30-μm-z-projections of a capillary pre- and post irradiation and occlusion with corresponding position of line scans (yellow = irradiation scan, cyan = flow scan). The line scan kymographs (shown within cyan rectangles, x = distance, t = time) confirm the presence (*Top*) or absence (*Bottom*) of blood flow. (Scale bar, 10 μm.) (*C*) Sequential line scan kymographs depicting a gradual reduction of blood flow to the point of full cessation at 70 s from the irradiation scan. (*D*) Duration of irradiation required to induce occlusion, with individual points representing individual capillaries (N = 3, n = 19). Mean ± SEM. (*E*) *Left*: Representative third harmonic generation (THG) images with the corresponding line scan kymographs (shown within cyan rectangles; x = distance, t = time) obtained in the absence of any dye. (Scale bar, 10 μm.) *Right*: No reduction in blood flow was detected (n.s., two-tailed paired *t* test; N = 3, n = 11). (*F*) *Left*: Control experiments using dextran-bound dyes (70 kDa) with the corresponding flow scans (shown within cyan rectangles, x = distance, t = time). (Scale bar, 10 μm.) *Right*: No reduction in blood flow was detected: red points = Texas Red-dextran (70 kDa; N = 2, n = 9), green points = FITC-dextran (70 kDa; N = 1, n = 3) (n.s., two-tailed paired *t* test). (*G*) *Left*: Control experiments using quantum dots Qtracker655™ with the corresponding flow scans (shown within cyan rectangles, x = distance, t = time). (Scale bar, 10 μm.) *Right*: No reduction in blood flow was detected (n.s., two-tailed paired *t* test; N = 4, n = 13). N = number of animals, n = number of capillaries. n.s. = not significant.

(*SI Appendix,* Fig. S2 *H* and *J*). However, following intravenous injection, the fluorescence of *Ps2P* remained stable throughout the imaging period, whereas Rose Bengal was rapidly cleared from the vasculature, as evidenced by a steep decline in its fluorescence within 5 to 10 min after injection (*SI Appendix,* Fig. S2 *A* and *B*). Substantially longer vascular retention, appropriate for carrying out multiple occlusions and ensuing compatibility with longitudinal imaging are other distinct advantages of *Ps2P*. Importantly, irradiation at 1040 nm in the absence of *Ps2P* or Rose Bengal did not induce capillary occlusion or alter $V_{RBC}$ (*SI Appendix,* Fig. S2*D*).

**Irradiation in the Presence of *Ps2P* Leads to Blood Flow Stalling and EC Injury, but Not Clot Formation.** Next, we sought to gain insight into the mechanism behind capillary blood flow stalls induced by photodynamic treatment using *Ps2P*. Vascular occlusions are commonly driven by i) thrombus formation, particularly in large vessels, or ii) stalling of blood cells in brain capillaries (6, 7, 10, 13, 14, 41). First, we tested whether capillaries irradiated in the presence of *Ps2P* showed signs of platelet activation or fibrin aggregation. Animals were pretreated with anticoagulants, such as aspirin, heparin, or clopidogrel, before irradiation, assuming that if stalling were to occur as a result of thrombus formation, anticoagulants would reduce its occurrence. However, capillary occlusion occurred in 90% of aspirin-, 94% of heparin-, and 100% of clopidogrel-treated capillaries (Fig. 3 *A* and *B*). Furthermore, we tested whether a recombinant tissue plasminogen activator (rtPA), an U.S. Food and Drug Administration-approved thrombolytic drug, injected 30 min after the occlusion, could restore blood flow. In all cases, rtPA did not lead to capillary recanalization, confirming that capillary stalls in our model are not due to fibrin-driven intravascular clot formation (Fig. 3 *A* and *B*).

Next, we tested whether capillary stalls were caused by a specific type of transiting cells. Leukocytes, platelets, and RBCs were labeled using well-established cellular markers Rhodamine 6G, Hoechst 33342, and Alexa Fluor 488 TER-119 (Fig. 3*C*). Leukocytes exhibited dual staining with Rhodamine 6G and Hoechst 33342 (6); platelets were stained with Rhodamine 6G only, and RBCs were labeled with Alexa Fluor 488 TER-119. In addition, Texas Red-dextran was injected to label the blood plasma. Subsequent capillary irradiation in the presence of *Ps2P* led to clogging of capillaries by individual cells, including leukocytes, RBCs, or platelets (Fig. 3*C*). However, the stalling cells were random, and no specific cell type could be identified as the cause of the occlusion. Instead, upon irradiation and the resulting decrease in blood flow, transiting cells became lodged in the capillary segment adjacent to the irradiation site, contributing to the resulting capillary occlusion.

Having demonstrated that capillary occlusion in our model does not result from classical intravascular coagulation pathways, we turned our attention to vessel wall injury, specifically endothelial injury, as a potential underlying mechanism. Using Claudin5-enhanced green fluorescent protein (EGFP) endothelial reporter mice, we analyzed EC morphology before and after irradiation. Indeed, we observed EC damage at the site of irradiation in the targeted capillary (Fig. 3 *D* and *E*), suggesting that the capillary occlusion was likely caused by local EC injury rather than by intravascular clot formation or blood cell stalling. Detailed observations

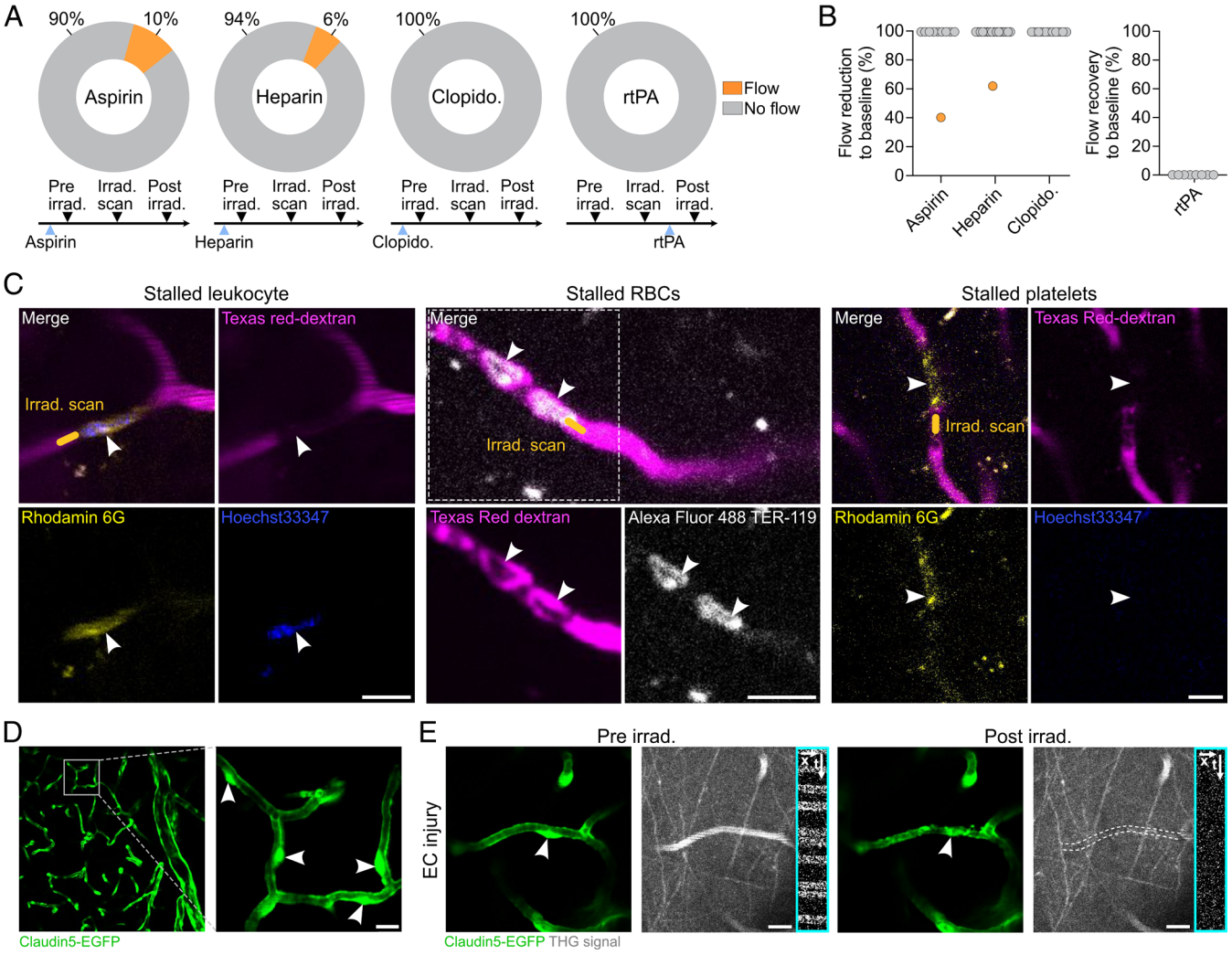


**Fig. 3.** (*A*) Quantification of patent capillaries subjected to irradiation in the presence of *Ps2P*, either pretreated with anticoagulants to prevent occlusion or posttreated with rtPA to promote recanalization. All treatments failed to prevent blood flow cessation or to restore blood flow, respectively. (*B*) Reduction in blood flow upon capillary irradiation in the presence of anticoagulant drugs (*Left*): Aspirin (N = 2, n = 10), heparin (N = 3, n = 17), clopidogrel (N = 4, n = 11) or blood flow recovery following reperfusion therapy with rtPA (N = 2, n = 8; *Right*). Points represent single capillaries. (*C*) Representative 2P images showing stalled blood cells inside the targeted capillary [*Left*: leukocyte, *Middle*: RBCs, *Right*: platelets]. Channels are displayed separately, with the merged image in the *Top Left*. (Scale bar, 10 μm.) (*D*) Representative maximum intensity 2P 10-μm-z-projections of a Claudin5-enhanced green fluorescent protein (EGFP) reporter mouse. White arrowheads indicate individual EC nuclei. (Scale bar, 10 μm.) (*E*) Representative 2P images of an EC injured capillary, showing pre irradiation EC morphology (*Left*) and post irradiation damage (*Right*). Line scan kymographs (cyan rectangles) using THG imaging confirm the presence and absence of blood flow pre- and post irradiation, respectively. Dashed lines indicate location of blood flow before occlusion. White arrowheads point toward EC nuclei. (Scale bar, 10 μm.) N = number of animals, n = number of capillaries.

related to EC injury and the associated capillary outcomes are presented in a separate article (42).

**Consequences of Single Capillary Injury: Capillary Recanalization, Changes in Local Hemodynamics, $pO_2$, and Microglial Activation.** To study the fate of the damaged capillaries, we performed longitudinal 2P imaging of the adjacent microvascular network directly after induction of occlusion, as well as 24 h and 48 h post irradiation. Remarkably, blood flow was restored in all targeted capillaries 24 to 48 h post irradiation, revealing a rapid brain capillary repair response (Fig. 4 *A* and *B*).

Capillary flow stalls may lead to changes in perfusion, oxygenation, and neuroinflammation in the affected area. To date, research on brain capillary stalls and injury has primarily focused on multiple and widespread capillary occlusions (6, 13, 17, 18), while the effects of single capillary occlusions remain largely unknown. ECgo provides a valuable tool for manipulating one brain capillary at a time in order to assess local hemodynamics, tissue oxygenation, and microglial responses.

To evaluate the impact of capillary occlusion and subsequent repair on local tissue oxygenation, we used Oxyphor 2P, a previously developed $pO_2$ sensor (25), and 2P phosphorescence lifetime microscopy (43, 44) to image the $pO_2$ distribution in the area adjacent to the occlusion in awake animals, as described previously (45). $pO_2$ in the surrounding tissue was measured prior to the induction of occlusion (baseline $pO_2$), 30 min, 24 h, and 48 h post irradiation (Fig. 4*C*). Within the examined two-dimensional circular region (50 μm in diameter) surrounding the occlusion site (Fig. 4*D*), the mean tissue $pO_2$ showed a clear transient downward trend immediately after the occlusion, decreasing by 26.6% (from 29.1 mmHg to 21.4 mmHg); however, this change was not statistically significant in our dataset. The mean tissue $pO_2$ returned to the baseline level within 24 to 48 h upon blood flow recovery (Fig. 4*D*). Notably, the observed $pO_2$ drop did not reach hypoxic levels (<10 mmHg), indicating that the

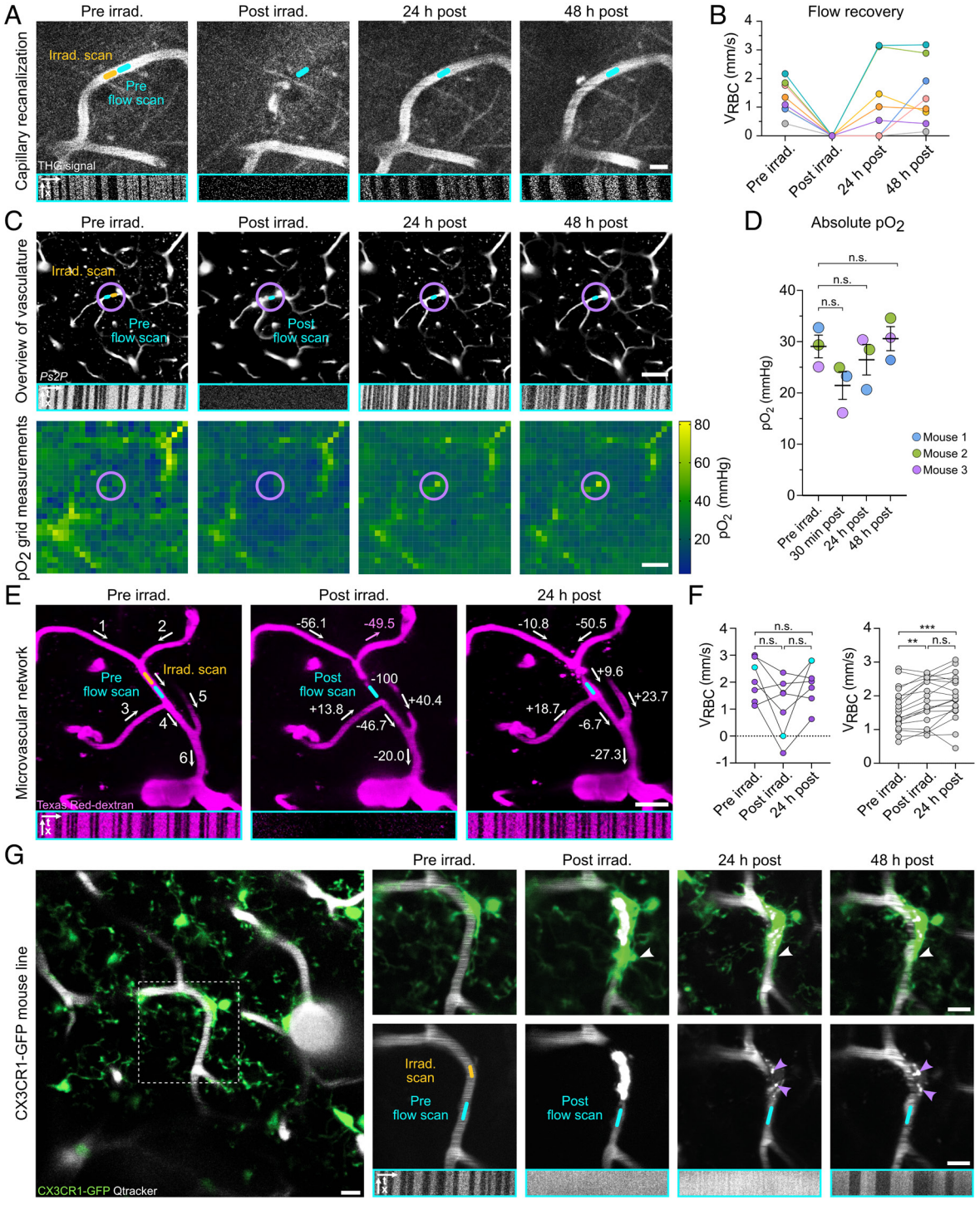


**Fig. 4.** (*A*) Representative 2P images showing capillary recanalization 24 h post irradiation with corresponding line-scan kymographs (cyan rectangle, *Bottom*). THG = third-harmonic generation. (*B*) Quantification of $V_{RBC}$ recovery 24 h and 48 h post irradiation. Each point represents an individual capillary (N = 3, n = 8). (*C*) Local tissue partial pressure of oxygen ($pO_2$) pre- and post irradiation. *Top* panels: Two-photon images of the region of interest surrounding the occluded capillary recorded pre irradiation, immediately post irradiation, as well as 24 h and 48 h post irradiation, with the corresponding line-scan kymographs (shown within cyan rectangle). *Bottom* panels: 28 × 28 grid-like measurements of tissue $pO_2$ in awake mice performed pre irradiation, immediately post irradiation, as well as 24 h and 48 h post irradiation. The magenta circle (50 μm radius) marks the region quantified in *D*. (Scale bar, 50 μm.) (*D*) Absolute $pO_2$ values within the circular region shown in *C*. Each data point represents a single capillary occlusion (one occlusion per mouse), where different colors correspond to individual animals (N = 3, n = 3). Mean ± SD, $P > 0.05$, Friedman test. (*E*) Local blood flow changes induced by single capillary occlusion. Maximum-intensity 2P 30 μm z-projections with the corresponding line-scan kymographs (shown within cyan rectangles, *Bottom*). Numbers indicate neighboring capillary segments. Relative RBC velocity ($V_{RBC}$) changes in neighboring capillaries (1 to 5) post irradiation. (Scale bar, 10 μm.) (*F*) *Left*: Quantification of $V_{RBC}$ in capillaries pre- and post irradiation from the example in *E* (N = 1, n = 7). *Right*: Quantification of $V_{RBC}$ in the adjacent microvascular network (N = 1, n = 19). The occluded capillary is shown in cyan. Magenta points represent adjacent capillaries (capillaries 1 to 6 in *E*), while gray points correspond to capillary segments in the surrounding microvascular network that are not directly attached to the occluded capillary and not shown in the z-stack projection. *$P < 0.05$, repeatedly measured one-way ANOVA. Mean ± SEM. (*G*) Microglial response to capillary occlusion. *Top* panels: local microglial activation post irradiation in CX3CR1-GFP reporter mouse, with microglial processes ensheathing the injured capillary (white arrowheads). *Bottom* panels: images of the fluorescence of an intravascular dye (Qtracker655™ pre- and post irradiation, Texas Red-dextran 24 h and 48 h post irradiation), showing the presence or absence of the blood flow in the targeted capillary pre- and post irradiation. 48 h after irradiation, the capillary is reinstated. Magenta arrowheads indicate internalized vascular dye. (Scale bar, 10 μm.) N = number of animals, n = number of capillaries.

surrounding microvascular network was able to compensate for the local damage and maintain oxygen delivery to tissue.

Next, we examined how the occlusion of a single capillary impacts hemodynamics in the surrounding capillary network. A selected capillary was irradiated, and $V_{RBC}$ was measured in the adjacent capillaries. Following the occlusion, the blood flow in the directly connected branches (the two feeding capillaries and the single draining capillary) was reduced (capillaries 1, 2, and 4 in Fig. 4*E*). The analysis of the flow in the wider capillary network surrounding the occlusion revealed that overall $V_{RBC}$ in the affected area increased (Fig. 4*F*), suggesting that upon a single capillary occlusion, the collateral flow compensates for the local perfusion deficit. Importantly, our data show that while the blood flow ceased in the targeted capillary, neighboring vessels remained patent, highlighting the robustness of the cortical capillary network and suggesting the presence of a mechanism that signals the adjacent network to compensate for single capillary occlusion.

Resident microglia are known to react rapidly to local cell damage (46–48) and vascular injury (11, 21, 49). To test whether capillary injury in our model led to a local inflammatory response and subsequent microglial activation, we used CX3CR1-GFP transgenic reporter mice. We observed that microglia became locally activated after the capillary injury, extended their processes to ensheathe the injured capillary, and internalized the leaked vascular probe Qtracker655™, as indicated by coexpression of vascular and GFP signals (Fig. 4*G*). While we did not observe capillary rupture or extensive bleeding, we occasionally detected spatially confined extravasation of blood plasma tracers near the targeted capillary segment, consistent with transient barrier disturbances at the site of the injured EC. This microglial activation was seen both in cells directly next to the occluded capillary (Fig. 4*G*) and nearby microglia that were not in direct contact with it, suggesting that local inflammatory signaling occurs in response to EC injury.

## Discussion

Here, we have introduced a porphyrin-based photosensitizer, *Ps2P*, and demonstrated its use for induction of single-EC injury and capillary occlusion in the living brain under 2P excitation, an approach termed ECgo. The most important feature of ECgo is that it allows for a highly accurate single capillary occlusion, avoiding vessel rupture and collateral damage to neighboring vessels and tissue. Interestingly, the damaged capillaries were found to undergo fast repair and regain blood flow within 24 to 48 h after injury. This time course is consistent with prior reports (11, 17, 18), while the ECgo method extends these observations by enabling selective targeting of individual capillaries with well-defined baseline measurements and longitudinal follow-up. Detailed investigation of this remarkable endothelial-mediated capillary repair is the focus of a separate study (42). Overall, ECgo provides a useful tool for studying the effects of single capillary injury on local blood flow, oxygenation, and neuroinflammatory responses.

Photodynamic methods have been used previously to create capillary occlusions. Perhaps the most-known photosensitizer is Rose Bengal (50), which is widely used for producing large vessel occlusions (1, 3–5, 51). In a direct side-by-side comparison (matched excitation efficiency at 1040 nm), both Rose Bengal and *Ps2P* were found to be capable of inducing capillary occlusions. However, Rose Bengal was cleared from the vasculature rapidly (within 5 to 10 min), limiting the effective time window for capillary targeting to a few minutes after injection, consistent with previous reports (47, 48). In contrast, *Ps2P* exhibited substantially longer vascular retention, enabling multiple independent capillary occlusions to be performed within a single imaging session without reinjection. In addition, *Ps2P* could be administered at ~20 times lower concentrations than Rose Bengal to achieve the same excitation efficiency, potentially reducing the risk of systemic or local side effects. Together, these features establish *Ps2P* as a useful tool for manipulation of individual brain capillaries in the living mouse brain in combination with long-term repeated imaging, complementing other approaches for inducing capillary injury.

In the ECgo paradigm, capillary occlusion arises from a localized EC injury rather than from a persistent intravascular clot (Fig. 3). Functional manipulations suggest that fibrin-based clotting does not play a major role in ECgo-induced capillary occlusion, as neither anticoagulant nor fibrinolytic treatments prevented occlusion or restored flow. Future studies incorporating fibrin visualization could provide additional support for this conclusion.

Together, these observations raise the question: what properties of *Ps2P* are responsible for its ability to induce such a precise single EC injury? A separate study would be required to delineate the exact mechanism of action of *Ps2P*; however, its relatively large aromatic structure and resulting hydrophobicity suggest that it could be partially distributed into the membranes and/or interiors of ECs that make up capillary walls. This contrasts with smaller, more hydrophilic sensitizers (e.g., Rose Bengal), which are presumably localized to the vascular lumen. Once associated with an EC and subjected to 2P excitation, *Ps2P* can operate via Type I and/or Type II photodynamic mechanisms (Fig. 1), leading to selective destruction of the targeted cell. Importantly, the excitation volume in which the triplet state of *Ps2P* is produced can be adjusted by regulating the photon flux (52), such that at mild excitation fluxes, the damage can be confined to a single EC. On the other hand, $^1O_2$ generated by *Ps2P* within the capillary lumen is expected to be scavenged by albumin molecules, to which *Ps2P* is likely to be bound. These partially damaged albumin molecules would be carried away and dispersed by the blood flow, not leading to the formation of a clot. The above scenario is speculative at this point, but it suggests a potentially testable hypothesis behind the highly selective action of *Ps2P*.

Capillary stalls are common for many cerebrovascular and neurodegenerative diseases (6–8, 13, 14). However, the development of reliable and precise techniques for inducing targeted single-capillary stalls in the rodent brain has remained an unmet challenge. Current approaches to induce capillary occlusion rely on the use of small occlusive materials, such as polymeric microbeads (17–19). However, such methods do not permit targeting of a single capillary in a preselected location. In contrast, the 2P photodynamic approach using *Ps2P* makes it possible to induce multiple, precisely targeted capillary occlusions one at a time at defined cortical depths, while avoiding widespread clot formation and/or systemic vascular damage, thereby enabling longitudinal in vivo imaging.

From a hemodynamic point of view, single capillary occlusions have been previously modeled in silico (53), demonstrating that changes in local capillary flow depend on baseline flow and local capillary network topology. Occlusion of a capillary segment with two inlet and two outlet vessels has the most severe impact on local tissue perfusion. In that case, blood flow is reduced by more than 30% in capillaries located within two branching orders from the occlusion site (53). Our current experimental results are in line with these modeling studies, showing that a single capillary occlusion causes redistribution of flow, suggesting that oxygen delivery is compensated by the local microvascular network. Indeed, while occlusion of a single capillary led to a drop in the tissue oxygenation in the area surrounding the capillary, $pO_2$ did not reach hypoxic levels. By exploiting the scalability of ECgo, which is one of its key advantages, occlusions of multiple capillaries could be induced to cause formation of local hypoxic regions, leading to tissue damage. How these microvascular events might contribute to long-term cerebrovascular impairment merits further investigation.

Single capillary occlusions contribute to neurodegenerative and cerebrovascular diseases, where progressive capillary dysfunction leads to chronic perfusion deficits (16, 54–56). Capillary occlusions and flow stops have been observed in aging (18, 19, 57), Alzheimer's disease (13, 14, 56), Type 1 diabetes (10, 11), and vascular dementia (12). ECgo makes it possible to create isolated capillary occlusions in an otherwise intact vascular network, enabling investigation of early microvascular dysfunction before the onset of widespread damage. Such studies are important to advance understanding of the vascular contribution to Alzheimer's disease and vascular dementia, where microvascular damage is thought to precede overt neurodegeneration (54, 56, 58).

Little is known about cellular and molecular responses to EC injury in the intact brain. Capillary repair and EC responses may vary across brain regions and conditions. Future studies will examine the impact of single capillary occlusions in different brain regions, aged animals, and disease states affecting the cerebrovasculature. Our preliminary results suggest that damaged capillaries exhibit rapid repair, though the mechanisms driving this process are still unclear. ECgo offers a valuable tool for studying capillary responses and outcomes following endothelial injury across pathophysiological contexts where maintaining vascular integrity is critical.

## Materials and Methods

***Ps2P* Synthesis.** *$H_2$TAPIP(GluOAll)$_8$.* To a solution of $H_2$TAPIP-OH (0.020 g, 0.011 mmol) in DMF (3 mL), HBTU (0.064 g, 0.168 mmol) was added, and the reaction mixture was stirred at room temperature (r.t.) for 10 min (*SI Appendix*, Fig. S1). N,N-diisopropylethylamine (0.088 mL, 0.504 mmol) and $NH_2$GluOAll·TsOH (0.067 g, 0.168 mmol) were added to the mixture, and the resulting solution was stirred at r.t. for 5 d. The reaction mixture was poured into an ice-cold aqueous solution of HCl (10%, 20 mL), and the green precipitate was collected by centrifugation, washed with water (2 × 10 mL), and dried in vacuum. The product was purified by silica gel column chromatography using dichloromethane (DCM):methanol (100:3) mixture as the eluent. The target compound was eluted as a green band. The solvent was removed by rotary evaporation, and the product (green solid) was dried in vacuum. Yield: 0.03 g (81%). $^1$H NMR (DMSO-$d_6$, 80 °C), δ (ppm): -2.10 (s, 2H), 1.87 to 1.94 (m, 32H), 2.14 to 2.25 (m, 32H), 4.15 to 4.22 (m, 24H), 4.42 to 4.54 (m, 32H), 4.96 to 5.09 (s, 32H), 5.63 to 5.74 (m, 14H), 6.94 (d, J = 8.65 Hz, 8H), 7.52 (t, J = 8.55 Hz, 4H), 7.83 (d, J = 6.45 Hz, 8H), 10.77 (s, 8H), 12.07 (s, 4H) (*SI Appendix*, Fig. S3).

*ZnTAPIP(GluOAll)$_8$.* To a solution of $H_2$TAPIP(GluOAll)$_8$ (0.03 g, 0.0084 mmol) in DMF (8 mL), an excess of $Zn(OAc)_2 \cdot 2H_2O$ (20 eq, 0.037 g, 0.168 mmol) was added, and the mixture was refluxed at 130 °C for 1 h. The reaction progress was monitored by measuring UV-vis absorption spectra. The mixture was cooled to r.t. and poured into ice-cold water. The resulting green precipitate was collected by centrifugation and dried in vacuum. Crude ZnTAPIP(GluOAll)$_8$ was introduced into the next step without further purification.

*Ps2P (ZnTAPIP(GluOH)$_8$).* ZnTAPIP(GluOAll)$_8$ (0.018 g, 0.0049 mmol) was dissolved in DMF (2 mL). $Pd(PPh_3)_4$ (0.046 g, 0.0395 mmol) and morpholine (0.34 mL, 3.92 mmol) were added, and the mixture was stirred for 48 h at r.t. The solvents were removed in vacuum, THF (10 mL) and acetic acid (0.5 mL) were added, and the resulting suspension was sonicated on an ultrasound bath for 10 min. The title compound was isolated by centrifugation as a green solid, washed with THF and then twice with $Et_2O$, and dried in vacuum. Yield: 0.014 g, 93%. $^1$H NMR (DMSO-$d_6$, 80 °C), δ (ppm): 1.89 to 1.97 (m, 32H), 2.18 to 2.27 (m, 32H), 3.58 to 3.61 (m, 32H), 4.15 to 4.20 (m, 24H), 6.93 (d, J = 8.40 Hz, 8H), 7.50 (t, J = 8.15 Hz, 4H), 7.72 to 7.56 (m, 16H), 7.83 to 7.89 (m, 16H), 10.69 (s, 8H), 11.88 (s, 4H), 14.66 (s, 16H) (*SI Appendix*, Fig. S4).

## Ethical Approval and Animal Welfare

This study was conducted following the Swiss Animal Protection Law and approved by the Swiss Veterinary Office, Canton of Zurich (Animal Welfare Act of December 16, 2005, and Animal Protection Ordinance of April 23, 2008). The local Cantonal Veterinary Office in Zurich granted ethical approval under licenses ZH169/2017 and ZH152/2021.

**Laboratory Animals.** This study utilized male and female mice between the ages of 2 and 8 mo. The animals were housed under a reversed 12:12 h light–dark cycle with unrestricted access to food and water. Standard laboratory chow was provided unless stated otherwise. Wild-type and control animals were C57BL/6 J mice obtained from Charles River. For the microglia studies, we employed CX3CR1-GFP mice (B6.129P-Cx3cr1/J; Jackson, Stock No.: 005582; Gensat.org). Investigations on ECs utilized Claudin5-EGFP mice (B6.Cg-Tg(Cldn5-EGFP) Cbet/U) (59, 60).

**In Vivo Two-Photon Imaging.** All 2P imaging experiments were performed using a custom-designed 2P laser scanning microscope (61). The system incorporated a femtosecond-pulsed laser (Chameleon Discovery TPC; Coherent/Spectra Physics) tunable in the range of 680 to 1300 nm. The pulse duration was approximately 120 fs at 80 MHz repetition rate. Imaging was conducted using either a 25× water-immersion objective (W Plan-Apochromat 25×/1.05 NA; Olympus) or a 20× water-immersion objective (W Plan-Apochromat 20×/1.0 NA; DIC VIS-IR; Zeiss). Emitted fluorescence was separated from the excitation light using an 825 nm short-pass (SP) dichroic mirror and further divided into four detection channels using additional dichroic mirrors (506, 560, and 652 nm). Each channel was equipped with specific SP and band-pass filter combinations: CH1 (770 SP + 475/64 BP), CH2 (770 SP + 535/50 BP), CH3 (770 SP + 607/70 BP), and CH4 (810 SP + 824 SP + 990 SP). Fluorescence signals were detected and amplified using photomultiplier tubes (PMTs; CH1–3: H10770PA-40 SEL, Hamamatsu; CH4: H10770PA-50 SEL, Hamamatsu). PMT gain was regulated via custom software written in LabVIEW. Image acquisition and system control were managed using a customized version of ScanImage r3.8.1 (62).

**Imaging of Cerebral Vasculature.** Animals underwent head plate surgery and chronic cranial window implantation to enable head fixation for subsequent 2P imaging (*SI Appendix*). The visualization of cortical blood vessels was achieved through the intravenous administration of fluorescent tracers. The choice of tracer depended on the mouse strain and its ability to express fluorescent proteins. Specifically, 50 µL of Texas Red-dextran (2.5% in aq. NaCl; 70 kDa; Thermo Fisher Scientific, D1830), FITC-dextran (2.5% in aq. NaCl; 70 kDa; Sigma; 46945-100MG-F), or 20 µL of Qtracker655™ (Thermo Fisher Scientific, Q21021MP) was injected.

**Blood Flow Measurements.** The assessment of blood flow velocity ($V_{RBC}$) was performed using line scans. RBC velocity was determined by performing a line scan along the vessel's midline (256 × 256 pixels; 0.64 ms per line; recorded over 72 frames, corresponding to 11.8 s). Subsequent analysis of the line scans was performed using a custom image processing toolbox [Cellular and Hemodynamics Processing Suite (63)] in conjunction with the RADON (64) transform in MATLAB (R2017b; MathWorks).

**Drug Application.** Intravenous injection of 0.2 IU/g Heparin (Heparin-Na; B. Braun) was performed via the tail vein a few minutes before capillary irradiation. Clopidogrel (Tocris, Cat.# 1820) administration included either a 4-d treatment at a lower dose (20 mg/kg; one i.p. injection per day over 4 d) or a higher single dose injection (100 mg/kg, i.p.) on the capillary irradiation day, with a minimum 3-h waiting period between injection and capillary irradiation. Aspirin application (100 mg/kg; Sigma, A5376) was performed through either i.p. or i.v. injection 3 h prior to capillary irradiation. For rtPA (Human t-PA; Actilyse; Boehringer Ingelheim)

administration, intravenous injection via the tail vein was performed post irradiation (10 mg/kg; 10% bolus; 90% perfusion; i.v.) (65). After starting the rtPA infusion, the targeted vasculature was monitored for at least 125 min to assess recanalization.

**In Vivo Staining of Blood Cells.** Cells within blood vessels were identified based on their morphology and staining patterns using Rhodamine 6G and Hoechst 33342. Blockages caused by RBCs appeared as dark, hollow areas, while platelets were observed as clusters of small green particles. Neutrophils were the only cells that exhibited double staining with Rhodamine 6G and Hoechst 33342 (6).

**Photothrombosis Using Rose Bengal.** Rose Bengal (20 mg/mL in saline; Thermo Fisher Scientific, A17053) was injected via a tail vein catheter. The dose of Rose Bengal was adjusted according to the difference between its 2PA cross-section and that of *Ps2P* at the excitation wavelength (1040 nm). Photoactivation was performed by line-scanning along the midline of the target vessel (time-averaged power 30 mW under the objective) until blood flow ceased.

**Data Analysis.** All 2P imaging data were processed using Fiji (Fiji Is Just ImageJ; ImageJ 2.1.0). The individual imaging channels were merged, and MIPs were generated following the specifications outlined in the figure legends. For images that were not quantitative, gamma values were adjusted nonlinearly to enhance the visibility of low-intensity structures. For quantitative fluorescence analyses, MIPs were generated in FIJI for each time point, and the fluorescence intensity was measured over time within a spatially stable region of interest. Brightness and contrast were autoadjusted on the first image of each series, and the same settings were applied uniformly to all subsequent images. Line scans were analyzed using a custom MATLAB image-processing toolbox (Cellular and Hemodynamic Image Processing Suite (63); R2014b; MathWorks) and blood flow velocity was calculated using the Radon transform algorithm (64). Graphical illustrations were created using Affinity Designer (Serif Europe, United Kingdom) and BioRender (BioRender, Toronto, Canada).

**Statistical Analysis.** Quantitative datasets were managed in Excel (Microsoft Corporation, Redmond, WA, United States), while statistical analyses were performed using GraphPad Prism (version 10.0; GraphPad Software, La Jolla, CA, United States). The statistical tests applied, along with the number of animals (N) and capillaries (n), are detailed in the figure legends. Data are presented as mean ± SEM. The D'Agostino–Pearson omnibus normality test was used to assess data distribution. For datasets that were found to be normally distributed, an unpaired or paired Student's *t* test was used to compare two groups. Nonnormally distributed data were analyzed using the Mann–Whitney test. Comparisons involving three groups were assessed using ANOVA or, for nonparametric data, the Kruskal–Wallis test (unpaired data) or the Friedman test (paired data), with Dunn's test applied for multiple comparisons.

**Data, Materials, and Software Availability.** All study data are included in the article and/or *SI Appendix* and have been deposited here: https://osf.io/qzdv3 (66).

**ACKNOWLEDGMENTS.** We thank the past and present laboratory members for their contributions to this project. We sincerely thank Christer Betsholtz for the Claudin5-EGFP mice. We also appreciate Lubor Borsig for providing CX3CR1-GFP mice and Ana Badimon and Anne Schäfer for donating clopidogrel. Thanks to Stefan Weber, Harald Osswald, Noemi Binini, and Anita Siebert for their support. B.W. was supported by the Swiss NSF (Grant numbers 310030_219656 and 310030_182703). M.D. was supported by the BRAIN NIH/NINDS Grant U24 NS109107 (Resource for Multiphoton Characterization of Genetically-Encoded Probes). S.A.V. acknowledges the support by the NIH/NIBIB Grants U24 EB028941 (Resource for Oxygen Imaging by Phosphorescence Quenching) and EB033877.

Author affiliations: [a]Institute of Pharmacology and Toxicology, University of Zurich, Zurich 8057, Switzerland; [b]Neuroscience Center Zurich, University and ETH Zurich, Zurich 8057, Switzerland; [c]Department of Biochemistry and Biophysics, Perelman School of Medicine, University of Pennsylvania, Philadelphia, PA 19104; [d]Department of Chemistry, School of Arts and Sciences, University of Pennsylvania, Philadelphia, PA 19104; [e]Department of Microbiology and Cell Biology, Montana State University, Bozeman, MT 59717; [f]G. Ciamician Department of Chemistry, University of Bologna, Bologna 40126, Italy; and [g]Department of Neurology, University Hospital Zurich, Zurich 8091, Switzerland

1. A. Lubart *et al.*, Single cortical microinfarcts lead to widespread microglia/macrophage migration along the white matter. *Cereb. Cortex.* **31**, 248–266 (2021).
2. J. Nguyen, N. Nishimura, R. N. Fetcho, C. Iadecola, C. B. Schaffer, Occlusion of cortical ascending venules causes blood flow decreases, reversals in flow direction, and vessel dilation in upstream capillaries. *J. Cereb. Blood Flow Metab. Off. J. Int. Soc. Cereb. Blood Flow Metab.* **31**, 2243–2254 (2011).
3. N. Nishimura, C. B. Schaffer, B. Friedman, P. D. Lyden, D. Kleinfeld, Penetrating arterioles are a bottleneck in the perfusion of neocortex. *Proc. Natl. Acad. Sci. U.S.A.* **104**, 365–370 (2007).
4. A. Y. Shih *et al.*, The smallest stroke: Occlusion of one penetrating vessel leads to infarction and a cognitive deficit. *Nat. Neurosci.* **16**, 55–63 (2013).
5. Z. J. Taylor *et al.*, Microvascular basis for growth of small infarcts following occlusion of single penetrating arterioles in mouse cortex. *J. Cereb. Blood Flow Metab.* **36**, 1357–1373 (2016).
6. M. El Amki *et al.*, Neutrophils obstructing brain capillaries are a major cause of no-reflow in ischemic stroke. *Cell Rep.* **33**, 108260 (2020).
7. ŞE. Erdener *et al.*, Dynamic capillary stalls in reperfused ischemic penumbra contribute to injury: A hyperacute role for neutrophils in persistent traffic jams. *J. Cereb. Blood Flow Metab.* **41**, 236–252 (2021).
8. A. Y. Shih, H. I. Hyacinth, D. A. Hartmann, S. J. Van Veluw, Rodent models of cerebral microinfarct and microhemorrhage. *Stroke* **49**, 803–810 (2018).
9. S. J. van Veluw *et al.*, Detection, risk factors, and functional consequences of cerebral microinfarcts. *Lancet Neurol.* **16**, 730–740 (2017).
10. S. Sharma *et al.*, A pathogenic role for IL-10 signalling in capillary stalling and cognitive impairment in type 1 diabetes. *Nat. Metab.* **6**, 2082–2099 (2024).
11. E. M. F. Mehina *et al.*, Invasion of phagocytic galectin 3 expressing macrophages in the diabetic brain disrupts vascular repair. *Sci. Adv.* **7**, eabg2712 (2021).
12. J.-H. Yoon *et al.*, Increased capillary stalling is associated with endothelial glycocalyx loss in subcortical vascular dementia. *J. Cereb. Blood Flow Metab.* **42**, 1383–1397 (2022).
13. M. Ali *et al.*, VEGF signalling causes stalls in brain capillaries and reduces cerebral blood flow in Alzheimer's mice. *Brain* **145**, 1449–1463 (2022).
14. J. C. Cruz Hernández *et al.*, Neutrophil adhesion in brain capillaries reduces cortical blood flow and impairs memory function in Alzheimer's disease mouse models. *Nat. Neurosci.* **22**, 413–420 (2019).
15. W. R. Brown, C. R. Thore, Review: Cerebral microvascular pathology in ageing and neurodegeneration. *Neuropathol. Appl. Neurobiol.* **37**, 56–74 (2011).
16. A. R. Nelson, M. D. Sweeney, A. P. Sagare, B. V. Zlokovic, Neurovascular dysfunction and neurodegeneration in dementia and Alzheimer's disease. *Biochim. Biophys. Acta BBA–Mol. Basis Dis.* **1862**, 887–900 (2016).
17. P. Reeson, K. Choi, C. E. Brown, VEGF signaling regulates the fate of obstructed capillaries in mouse cortex. *Elife* **7**, e33670 (2018).
18. P. Reeson, B. Schager, M. Van Sprengel, C. E. Brown, Behavioral and neural activity-dependent recanalization of plugged capillaries in the brain of adult and aged mice. *Front. Cell. Neurosci.* **16**, 876746 (2022).
19. B. Schager, C. E. Brown, Susceptibility to capillary plugging can predict brain region specific vessel loss with aging. *J. Cereb. Blood Flow Metab.* **40**, 2475–2490 (2020).
20. S. K. Bonney, C. D. Nielson, M. J. Sosa, O. Bonnar, A. Y. Shih, Capillary regression leads to sustained local hypoperfusion by inducing constriction of upstream transitional vessels. *Proc. Natl. Acad. Sci. U.S.A.* **121**, e2321021121 (2024).
21. S. Taylor *et al.*, Suppressing interferon-γ stimulates microglial responses and repair of microbleeds in the diabetic brain. *J. Neurosci.* **38**, 8707–8722 (2018).
22. P. Delafontaine-Martel *et al.*, Targeted capillary photothrombosis via multiphoton excitation of rose bengal. *J. Cereb. Blood Flow Metab.* **43**, 1713–1725 (2023).
23. M. Fukuda, T. Matsumara, T. Suda, H. Hirase, Depth-targeted intracortical microstroke by two-photon photothrombosis in rodent brain. *Neurophotonics* **9**, 021910 (2022).
24. L. Zhu *et al.*, Single-microvessel occlusion produces lamina-specific microvascular flow vasodynamics and signs of neurodegenerative change. *Cell Rep.* **42**, 112469 (2023).
25. T. V. Esipova *et al.*, Oxyphor 2p: A high-performance probe for deep-tissue longitudinal oxygen imaging. *Cell Metab.* **29**, 736–744.e7 (2019).
26. J. F. Algorri, M. Ochoa, P. Roldán-Varona, L. Rodríguez-Cobo, J. M. López-Higuera, Photodynamic therapy: A compendium of latest reviews. *Cancers* **13**, 4447 (2021).
27. J. H. Correia, J. A. Rodrigues, S. Pimenta, T. Dong, Z. Yang, Photodynamic therapy review: Principles, photosensitizers, applications, and future directions. *Pharmaceutics* **13**, 1332 (2021).
28. T. C. Pham, V.-N. Nguyen, Y. Choi, S. Lee, J. Yoon, Recent strategies to develop innovative photosensitizers for enhanced photodynamic therapy. *Chem. Rev.* **121**, 13454–13619 (2021).
29. M. Bregnhøj, M. Westberg, F. Jensen, P. R. Ogilby, Solvent-dependent singlet oxygen lifetimes: Temperature effects implicate tunneling and charge-transfer interactions. *Phys. Chem. Chem. Phys.* **18**, 22946–22961 (2016).

30. A. Soleimany *et al.*, Two-photon mediated cancer therapy: A comprehensive review on two-photon photodynamic therapy and two-photon–activated therapeutic delivery systems. *Adv. Funct. Mater.* **34**, 2408594 (2024).
31. V. Juvekar *et al.*, Two-photon excitation photosensitizers for photodynamic therapy: From small-molecules to nano-complex systems. *Coord. Chem. Rev.* **506**, 215711 (2024).
32. S. M. S. Kazmi *et al.*, Three-dimensional mapping of oxygen tension in cortical arterioles before and after occlusion. *Biomed. Opt. Express* **4**, 1061–1073 (2013).
33. A. Srivatsan, J. R. Missert, S. K. Upadhyay, R. K. Pandey, Porphyrin-based photosensitizers and the corresponding multifunctional nanoplatforms for cancer-imaging and phototherapy. *J. Porphyrins Phthalocyanines* **19**, 109–134 (2015).
34. H. A. Collins *et al.*, Blood-vessel closure using photosensitizers engineered for two-photon excitation. *Nat. Photonics* **2**, 420–424 (2008).
35. T. V. Esipova, H. J. Rivera-Jacquez, B. Weber, A. E. Masunov, S. A. Vinogradov, Two-photon absorbing phosphorescent metalloporphyrins: Effects of π-extension and peripheral substitution. *J. Am. Chem. Soc.* **138**, 15648–15662 (2016).
36. T. V. Esipova, H. J. Rivera-Jacquez, B. Weber, A. E. Masunov, S. A. Vinogradov, Stabilizing g-states in centrosymmetric tetrapyrroles: Two-photon-absorbing porphyrins with bright phosphorescence. *J. Phys. Chem. A* **121**, 6243–6255 (2017).
37. L. Ravotto *et al.*, Three-photon spectroscopy of porphyrins. *J. Phys. Chem. A* **124**, 11038–11050 (2020).
38. F. Wilkinson, W. P. Helman, A. B. Ross, Quantum yields for the photosensitized formation of the lowest electronically excited singlet state of molecular oxygen in solution. *J. Phys. Chem. Ref. Data* **22**, 113–262 (1993).
39. S. J. Ahn *et al.*, Label-free assessment of hemodynamics in individual cortical brain vessels using third harmonic generation microscopy. *Biomed. Opt. Express* **11**, 2665 (2020).
40. S. Dietzel *et al.*, Label-free determination of hemodynamic parameters in the microcirculaton with third harmonic generation microscopy. *PLoS One* **9**, e99615 (2014).
41. Ş. E. Erdener *et al.*, Spatio-temporal dynamics of cerebral capillary segments with stalling red blood cells. *J. Cereb. Blood Flow Metab.* **39**, 886–900 (2019).
42. J. Condrau *et al.*, Intrinsic endothelial remodeling drives brain capillary repair. *Neuron*, in press.
43. O. S. Finikova *et al.*, Oxygen microscopy by two-photon-excited phosphorescence. *Chemphyschem* **9**, 1673–1679 (2008).
44. S. Sakadžić *et al.*, Two-photon high-resolution measurement of partial pressure of oxygen in cerebral vasculature and tissue. *Nat. Methods* **7**, 755–759 (2010).
45. E. Erlebach *et al.*, Measurement of cerebral oxygen pressure in living mice by two-photon phosphorescence lifetime microscopy. *STAR Protoc.* **3**, 101370 (2022).
46. E. Császár *et al.*, Microglia modulate blood flow, neurovascular coupling, and hypoperfusion via purinergic actions. *J. Exp. Med.* **219**, e20211071 (2022).
47. D. Davalos *et al.*, ATP mediates rapid microglial response to local brain injury in vivo. *Nat. Neurosci.* **8**, 752–758 (2005).
48. A. Nimmerjahn, F. Kirchhoff, F. Helmchen, Resting microglial cells are highly dynamic surveillants of brain parenchyma in vivo. *Science* **308**, 1314–1318 (2005).
49. S. K. Halder, R. Milner, A critical role for microglia in maintaining vascular integrity in the hypoxic spinal cord. *Proc. Natl. Acad. Sci. U.S.A.* **116**, 26029–26037 (2019).
50. B. D. Watson, W. D. Dietrich, R. Busto, M. S. Wachtel, M. D. Ginsberg, Induction of reproducible brain infarction by photochemically initiated thrombosis. *Ann. Neurol.* **17**, 497–504 (1985).
51. C. B. Schaffer *et al.*, Two-photon imaging of cortical surface microvessels reveals a robust redistribution in blood flow after vascular occlusion. *PLoS Biol.* **4**, e22 (2006).
52. L. E. Sinks *et al.*, Two-photon microscopy of oxygen: Polymersomes as probe carrier vehicles. *J. Phys. Chem. B* **114**, 14373–14382 (2010).
53. F. Schmid, G. Conti, P. Jenny, B. Weber, The severity of microstrokes depends on local vascular topology and baseline perfusion. *Elife* **10**, e60208 (2021).
54. E. Farkas, P. G. M. Luiten, Cerebral microvascular pathology in aging and Alzheimer's disease. *Prog. Neurobiol.* **64**, 575–611 (2001).
55. L. S. Madsen *et al.*, Capillary dysfunction correlates with cortical amyloid load in early Alzheimer's disease. *Neurobiol. Aging* **123**, 1–9 (2023).
56. R. Nortley *et al.*, Amyloid β oligomers constrict human capillaries in Alzheimer's disease via signaling to pericytes. *Science* **365**, eaav9518 (2019).
57. A.-A. Berthiaume *et al.*, Pericyte remodeling is deficient in the aged brain and contributes to impaired capillary flow and structure. *Nat. Commun.* **13**, 5912 (2022).
58. C. Iadecola, The neurovascular unit coming of age: A journey through neurovascular coupling in health and disease. *Neuron* **96**, 17–42 (2017).
59. N. Honkura *et al.*, Intravital imaging-based analysis tools for vessel identification and assessment of concurrent dynamic vascular events. *Nat. Commun.* **9**, 2746 (2018).
60. L. Stanczuk *et al.*, CKit lineage hemogenic endothelium-derived cells contribute to mesenteric lymphatic vessels. *Cell Rep.* **10**, 1708–1721 (2015).
61. J. M. Mayrhofer *et al.*, Design and performance of an ultra-flexible two-photon microscope for in vivo research. *Biomed. Opt. Express* **6**, 4228 (2015).
62. T. A. Pologruto, B. L. Sabatini, K. Svoboda, Scanimage: Flexible software for operating laser scanning microscopes. *Biomed. Eng. OnLine* **2**, 13 (2003).
63. M. J. P. Barrett, K. D. Ferrari, J. L. Stobart, M. Holub, B. Weber, CHIPS: An extensible toolbox for cellular and hemodynamic two-photon image analysis. *Neuroinformatics* **16**, 145–147 (2018).
64. P. J. Drew, P. Blinder, G. Cauwenberghs, A. Y. Shih, D. Kleinfeld, Rapid determination of particle velocity from space-time images using the Radon transform. *J. Comput. Neurosci.* **29**, 5–11 (2010).
65. N. F. Binder *et al.*, Leptomeningeal collaterals regulate reperfusion in ischemic stroke and rescue the brain from futile recanalization. *Neuron* **112**, 1456–1472.e6 (2024).
66. J. Condrau *et al.*, Data from "ECgo: All-Optical Induction of Single Endothelial Cell Injury and Capillary Occlusion in the Brain." OSF. https://osf.io/qzdv3. Deposited 30 April 2026.